JOM, Vol. 73, No. 9, 2021
https://doi.org/10.1007/s11837-021-04763-2

Alternating-Current Electrophoretic Deposition of Spinel Coatings on Porous Metallic Substrates for Solid Oxide Fuel Cell Applications

ZHIKUAN ZHU,[1] UDAY PAL,[1,2] SRIKANTH GOPALAN,[1,2] A. MOHAMMED HUSSAIN,[3] SONG DONG,[4] NILESH DALE,[3] YOSUKE FUKUYAMA,[4] and SOUMENDRA BASU [1,2,5]

1.—Department of Mechanical Engineering, Boston University, Boston, MA 02215, USA. 2.—Division of Materials Science and Engineering, Boston University, Brookline, MA 02446, USA. 3.—Nissan Technical Center North America (NTCNA), Farmington Hills, MI 48331, USA. 4.—Nissan Research Center, Nissan Motor Corporation Limited, Kanagawa 237-8523, Japan. 5.—e-mail: basu@bu.edu

The performance of solid oxide fuel cells (SOFCs) can be degraded by "chromium poisoning" where thermally grown Cr_2O_3 on metallic surfaces forms volatile Cr-containing species that are redeposited on active regions of the cathode. This phenomenon is further exacerbated for porous metallic interconnects and metal-supported electrodes due to their large surface-to-volume ratios. In this study, electrophoretic deposition (EPD) of $CuNi_{0.2}Mn_{1.8}O_4$ spinel powders on porous SUS430 metallic substrates using alternating current (AC) was explored. Two-step densification heat treatment was used to form a thin, uniform, protective spinel coating. The area-specific resistance (ASR) and weight gain were tracked during 100-h oxidation tests at 700°C in air. The results showed that, despite the considerable complexity of the sample shape, AC EPD was able to form a protective coating layer that significantly limited the growth rate of the thermally grown oxide (TGO) by reducing the k_g value by a factor of 25.

INTRODUCTION

Stainless steels, which form protective Cr_2O_3 thermally grown oxides, are widely used as interconnects in SOFC applications and also as electrodes in metal-supported SOFCs.[1,2] Metallic interconnects come in various forms, including dense plates with cross-channels, or as metal supports for cells, in either dense or porous form. Typically, for metal-supported cells, a much thinner anode is needed. The metal support has higher electrical conductivity than the traditional Ni/yttria-stabilized zirconia (YSZ) anode support, and exhibits good resistance to cyclic oxidation.[3–5] Among stainless steels, SUS430 alloy has become one of the most popular materials because of the good match of its coefficient of thermal expansion (CTE) with that of YSZ, a widely used electrolyte material in SOFCs. The cost of SUS 430 alloy is much lower compared with Ni- or Co-based alloys or ceramic materials. SUS 430 is also highly machinable.[2,6,7]

At high operating temperatures, thermally grown Cr_2O_3 and $MnCr_2O_4$ protective layers form on the surface of SUS430, providing a diffusion barrier to further oxidation. However, the formation of these oxides leads to higher area-specific resistance. Also, Cr-containing vapor species such as $CrO_3(g)$ and $CrO_2(OH)_2(g)$ are generated and then deposited at the porous cathode under operating conditions. This phenomenon is called Cr poisoning, which is one of the major reasons for SOFC performance degradation.[8–13] Many approaches have been pursued to mitigate Cr poisoning, including removing Cr-containing vapor species using a filter,[14,15] using more

(Received March 16, 2021; accepted June 8, 2021; published online June 16, 2021)

Cr-tolerant cathode materials,[11] and cleaning the deposited Cr-containing phases on the cathode using electrochemical methods,[16,17] among others.

Recently, significant research efforts have focused on electrophoretic deposition (EPD) as a means of depositing protective coatings on metallic interconnects.[18,19] EPD is a low-cost approach using relatively simple apparatus. Moreover, EPD provides good thickness control, and allows for deposition on both flat and curved surfaces, enabling coating deposition on substrates with complex shapes. Cu-Mn spinels and Mn-Co-based spinels have been widely explored as coating materials for metallic interconnects.[20–24] Previous work by our group showed that Ni-doped Cu-Mn spinel coatings exhibited better phase stability, and exhibited lower Cr diffusivity in the coating layer.[25] Both direct-current (DC) EPD and alternating-current (AC) EPD have been studied by different researchers. Compared with DC EPD, AC EPD results in a denser green body and a more uniform deposition layer.[26,27]

In this study, $CuNi_{0.2}Mn_{1.8}O_4$ spinel powders were fabricated and coated on porous SUS430 substrates using AC EPD. A two-step densification method was used after deposition. To evaluate the effectiveness of the protective coating layer, a 100-h oxidation test was carried out at 700°C in air. The area-specific resistance (ASR) and weight gain of the samples were tracked during oxidation. Microstructural changes in the coating were examined, and the Cr concentration profiles were measured. The results showed that, despite the considerable complexity of the sample shape, AC EPD could form a protective coating layer that limited Cr diffusion in the coating and significantly reduced the growth rate of the thermally grown oxide. To the best of the authors' knowledge, this is the first example of oxidation-resistant AC EPD coatings on porous metallic substrates for SOFC applications.

EXPERIMENTAL PROCEDURES

The glycine-nitrate combustion synthesis process (GNP) was used to fabricate fine and homogeneous $CuNi_{0.2}Mn_{1.8}O_4$ spinel powders.[28] Our previous work showed that using a glycine-to-nitrate molar ratio of 0.63 leads to an optimal combustion reaction. Proportional quantities of reactants were dissolved in deionized (DI) water, and after stirring for 10 min, a clear blue solution formed. The solution was heated on a hot plate at $\sim$ 90°C to evaporate excess water. The beaker was then covered with fine stainless-steel mesh to prevent ejection of fine powders that form during combustion, and the temperature of the hot plate was then set to 500°C. Heating tape was used around the beaker and set to 100°C to avoid water condensation on the beaker wall during the reaction. Spontaneous combustion and powder formation typically occurred before the set temperature was reached. The resulting powder was transferred to a box furnace and calcined in air for 2 h at 800°C to remove residues.[29,30]

To decrease the size of the spinel powder, it was dispersed in ethanol and ball milled using 0.05-mm YSZ balls in a SPEX Sample Prep 8000 M mixer/mill. After ball milling, the YSZ balls were removed by sieving. The powders were dispersed in an ethanol/acetone solution. After ultrasonically vibrating the powder solution for 15 min, iodine/ethanol solution was added to the suspension. I_2 reacts with acetone and releases H^+ ions that adhere to the spinel particles, making them positively charged. The suspension was then ultrasonically vibrated for 15 min to ensure thorough mixing and reaction.

An AC signal generation setup was designed in our laboratory, comprising a dual DC power supply, function generator, oscilloscope, signal transfer circuit, and small DC power supply for the transfer circuit. The setup can generate pulsed DC signals or AC signals with variable duty cycles and independently adjustable positive and negative voltages and time ratios. The output voltage ranges from −50 V to + 50V, and the frequency ranges from 10 Hz to 1000 Hz.

Porous SUS430 substrates with dimensions of 1 cm × 1 cm × 0.4 cm were used as the cathode, with a 6 cm × 5 cm × 0.1 cm Cu plate as the anode. The electrodes were immersed into the suspension of spinel powder. Before deposition, the sample within the suspension was placed in a vacuum chamber for 10 min to remove air bubbles. When a negative bias is applied to the cathode, the positively charged spinel particles migrate to the cathode due to electrostatic forces. The AC signal used for deposition is shown in Fig. 1. Note that, since the powder is positively charged (due to surface-adsorbed H^+), negative voltages correspond to the coating deposition mode while positive voltages correspond to the coating removal mode. The coatings were deposited for 15 min in total, and a magnetic stirrer was used to increase the powder mobility inside the substrate.

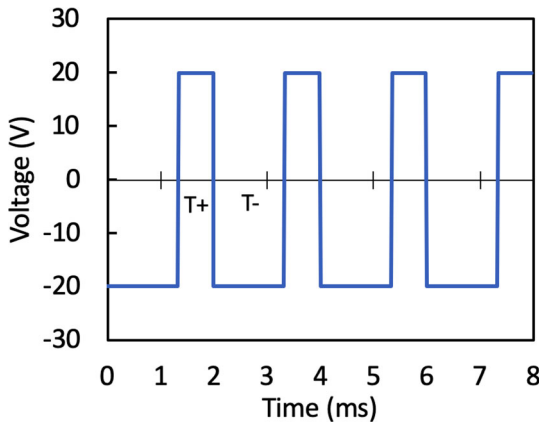

Fig. 1. AC signal used for deposition

To study the effectiveness of using AC EPD, a coated was also formed by DC EPD on a reference sample, using a –20 V DC signal for 3 min.

The as-deposited coatings need further densification. A two-step heat treatment was used for densification, consisting of a reduction anneal followed by a reoxidation anneal, as shown in Fig. 2.[31] As-deposited samples were reduced at 950°C for 2 h in pure H_2, during which the spinel is reduced to Cu-Ni alloy and manganese oxide. The sample was then cooled to room temperature then annealed in air at 750°C for 24 h, leading to a denser $CuNi_{0.2}Mn_{1.8}O_4$ spinel coating.

Oxidation tests were carried out on both uncoated and AC EPD-coated samples at 700°C for 100 h in air. During the oxidation exposure, thermogravimetric (TGA, TA Q600 microbalance) measurements were also carried out and the weight changes of both samples were continuously recorded. In addition, area-specific resistance (ASR) measurements were separately carried out for 100 h exposure at 700°C in air, using a four-quadrant power potentiostat (Zahner PP211). For these measurements, silver mesh and paste were applied on both sides of sample, and the potential was tracked when a 0.2 A current was applied. Note that the coated samples used for TGA and ASR measurements were different but prepared under identical conditions.

Powder samples were examined by x-ray diffraction (XRD) analysis (Bruker D8 Advance) and scanning electron microscopy (SEM, Zeiss Supra 55 VP). Uncoated and coated samples at various stages were mounted in epoxy and polished in cross-section. Polished cross-sections were examined by SEM to track microstructure changes. Energy-dispersive spectroscopy (EDS, Oxford Instruments, High Wycombe, UK) was used in line scan and elementary mapping modes to analyze the compositional distribution in the coating.

RESULTS AND DISCUSSION

The microstructure of the powder before and after ball milling is shown in Fig. 3. After milling, the spinel powder was ~ 200 nm in size. To evaluate the quality and purity of the spinel powder, XRD analysis was carried out on the calcined powder. The results (Fig. 4) match with standard cubic spinel peaks. Neither CuO nor MnO peaks were observed, indicating that the spinel powder was phase pure.[29]

Figure 5a and b show SEM micrographs of samples as deposited by DC and AC EPD, respectively. Each images consists of two parts, with the top part of each image showing the microstructure in the middle areas of the porous samples, which the powder has to diffuse through connected pores to reach, whereas the bottom part of each image shows the microstructure near the surface of the porous samples, where the powder has easier access to near-surface pores. This figure shows that AC deposition can ensure that a significantly larger amount of powder enters inner pores without clogging the near surface pores. The DC EPD sample (Fig. 5a) shows a thick coating on the surface of the sample, which effectively clogs the surface pores, resulting in very little coverage of the surface of inner pores by the coating. In contrast, the coverage

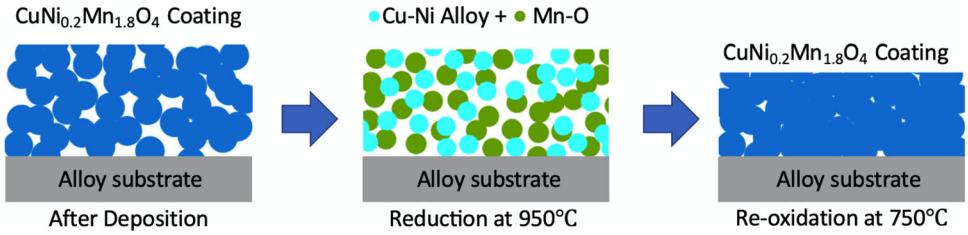

Fig. 2. Schematic illustration of microstructural development during two-step sintering heat treatment

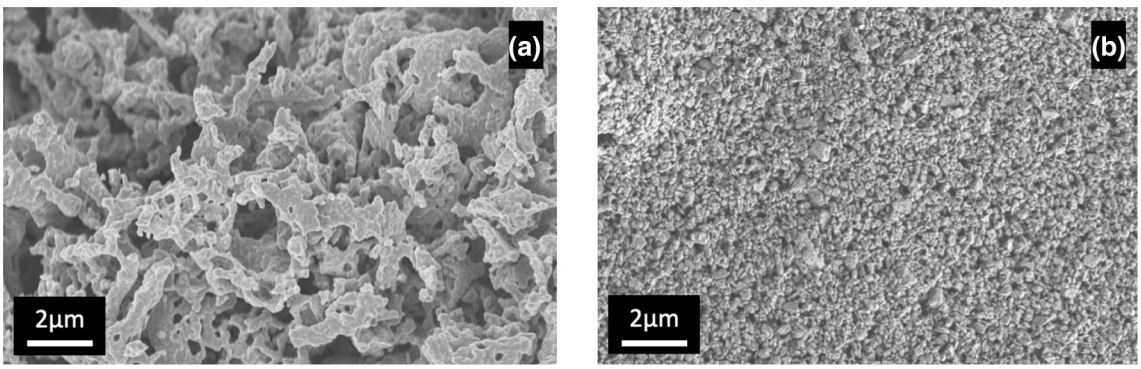

Fig. 3. Spinel powder samples (a) before and (b) after ball milling

after AC EPD deposition (Fig. 5b) is much more uniform. The surface of the sample is again coated, but without clogging the surface pores, thus allowing good coverage of the inner pores of the sample. This finding reveals that AC EPD is a much more effective deposition process for uniform coverage of porous substrates.

Figure 1 shows the AC voltage signal, with the −20 V signal corresponding to the deposition portion of the cycle and +20 V corresponding to the removal portion of the cycle. Since the deposition time is longer than the removal time, there is net deposition during each cycle. By alternating deposition and removal, the film thickness can be better controlled. Due to the excellent conductivity of the metallic interconnect, the voltage is fairly uniform in all parts of the porous substrate. As the coating has significantly lower electronic conductivity, the voltage drops rapidly in the coating as one moves away from the substrate–coating interface. Thus, if the coating gets thicker in one part of the sample compared with other areas, powder in the outer part of that area of the coating is most susceptible to removal during the +20 V exposure. This creates an autocorrecting mechanism that prevents the coating thickness in any portion of the sample from differing significantly from that in other parts. This keeps the surface pores open, which along with the stirring of the EPD solution allows powder to reach the inner pores of the sample.

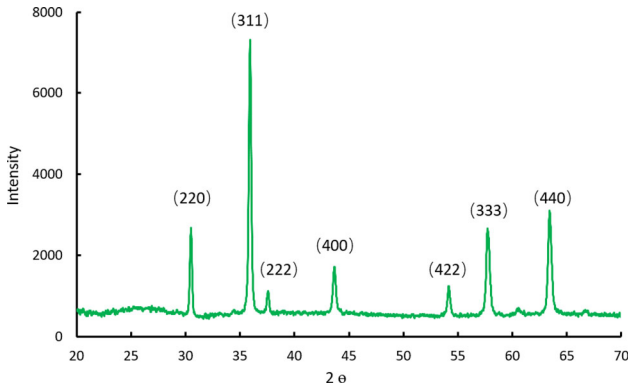

Fig. 4. XRD scan of $CuNi_{0.2}Mn_{1.8}O_4$ powder after calcination at 800°C in air

Figure 5c shows the microstructure of an AC EPD sample after two-step densification. A dense and uniform coating layer has formed on all the pore surfaces. This coating is expected to protect the porous SUS430 substrate from oxidation. Figure 6 shows a low-magnification SEM image of the AC EPD sample after the 100-h oxidation test and a randomly chosen zoomed-in area inside the substrate, with EDS maps of the constituent elements in the coating and substrate. The maps reveal the presence of the spinel coating on the surfaces throughout the pores. There is also a Cr-rich layer formed at SUS430 pore surfaces, probably formed during the densification process. However, the spinel coating covers the Cr layer and protects the substrate from further oxidization.

Due to the tortuous surface morphology of the substrate, the diffusion rate of spinel powder can differ from pore to pore. This makes it more challenging to deposit uniform coatings on porous than flat samples. However, the figure clearly shows that AC EPD enables reasonably uniform coverage of all pore surfaces in the sample, even for pores in the middle of the porous substrate.

Plots of the weight gain per unit area of the uncoated and coated samples as a function of oxidation time are shown in Fig. 7. The oxidation rate constant, k_g, was calculated for both samples.[32] The fits give k_g values of 2.25×10^{-6} mg^2 cm^{-4} s^{-1} for the uncoated sample and 9.0×10^{-8} mg^2 cm^{-4}

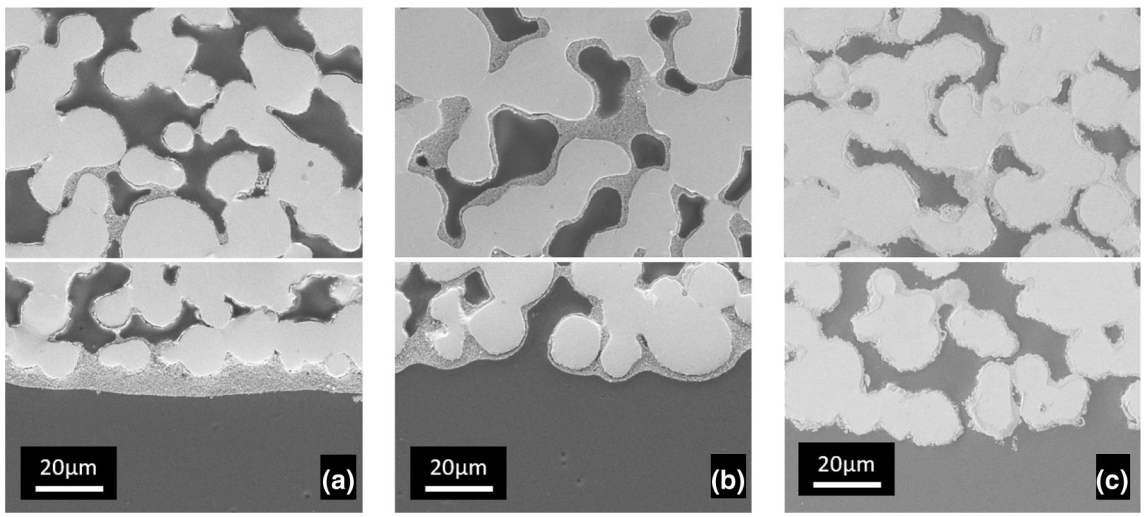

Fig. 5. SEM micrographs of cross-sections of (a) as-deposited DC EPD sample, (b) as-deposited AC EPD sample, and (c) AC EPD sample after two-step densification process. The top part of each image shows pores in the middle of the samples, while the bottom part shows near-surface pores

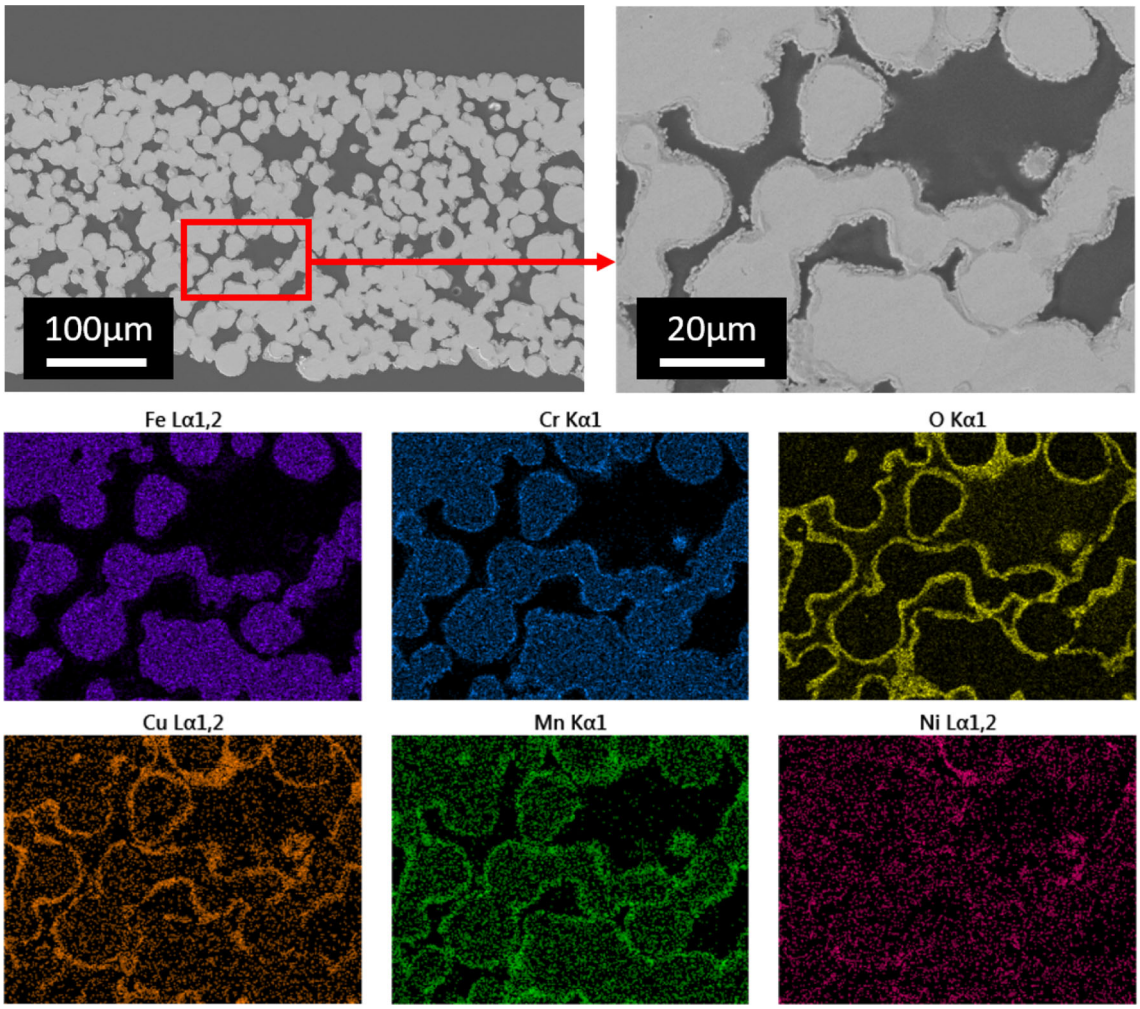

Fig. 6. Low-magnification SEM image, and EDS mapping of coated sample after two-step densification and 100-h oxidation test

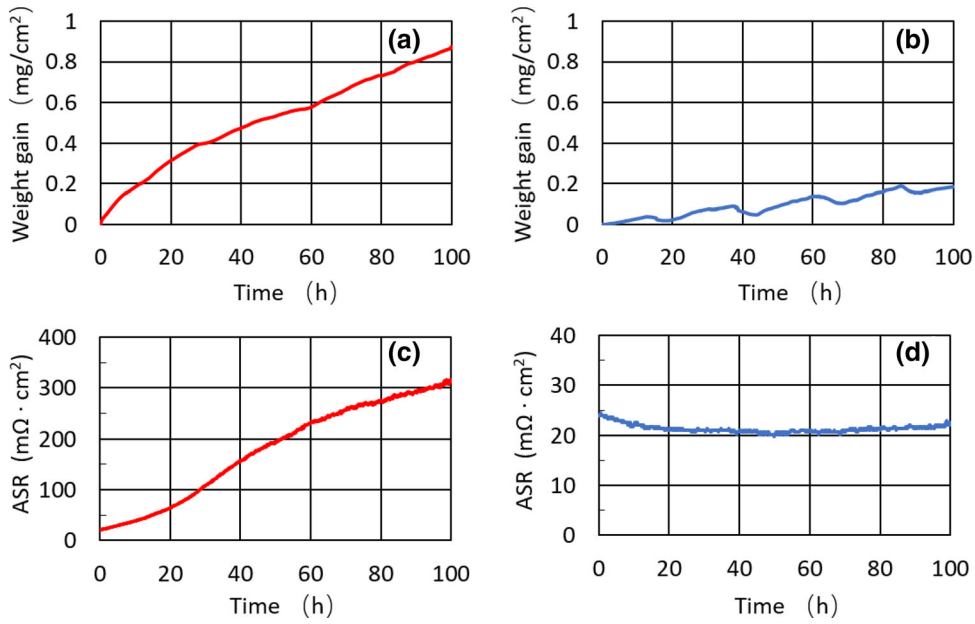

Fig. 7. Weight gain per unit area measured by thermogravimetry of (a) uncoated and (b) coated sample as a function of time. ASR changes as a function of time for (c) uncoated and (d) coated sample. All data measured at 700°C in air

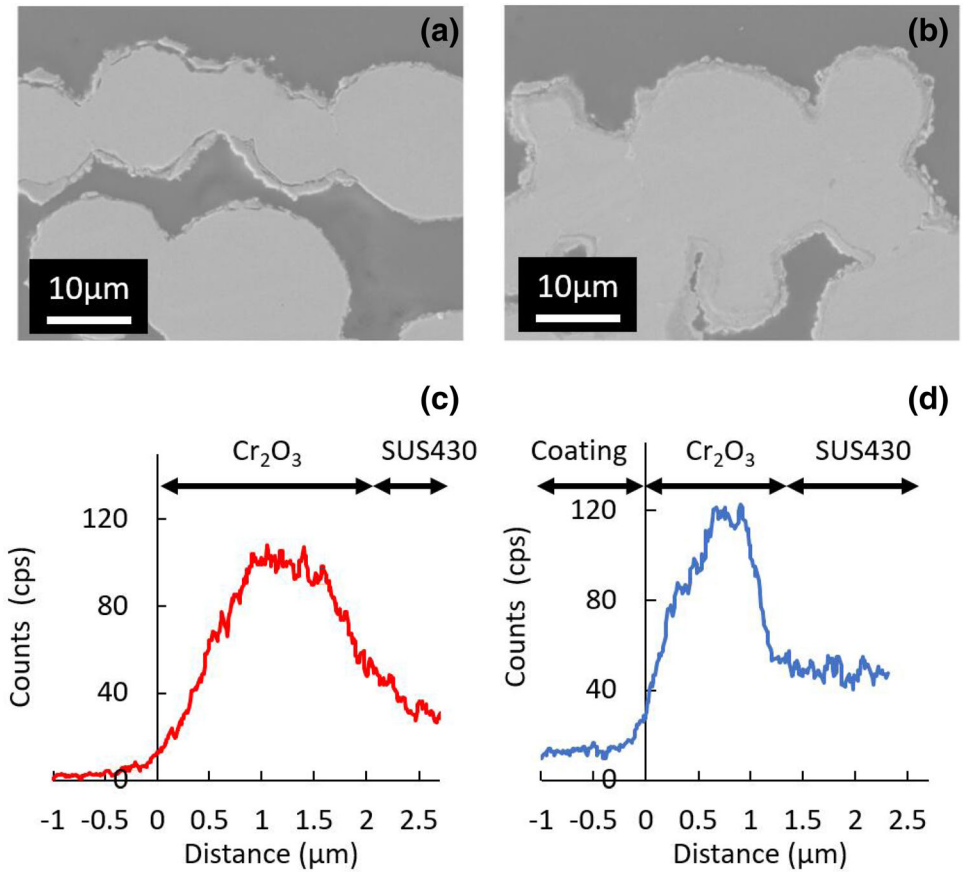

Fig. 8. SEM micrographs of cross-sections after 100-h oxidation test at 700°C in air of (a) uncoated and (b) coated sample. EDS line scans across the (c) TGO/substrate in the uncoated sample and (d) coating/TGO/substrate in the coated sample

s^{-1} for the coated sample, which corresponds to a factor of 25 improvement for the coated sample. Note that the area used here is the cross-sectional area of the sample, not the total surface area of the pores on which the coating is deposited. This means that the actual k_g values for both samples is smaller than reported here. However, since the data for both coated and uncoated samples are quantified in the same manner, their relative comparison is valid. The constant time period fluctuations in Fig. 7a and b are due to the variation in the room temperature from day to night, which changes the density of air and thus the buoyancy of the sample holder in the microbalance. These fluctuations are more obvious on the coated sample due to the smaller total weight gain.

Figure 7c and d shows the ASR changes during the 100-h exposure in air at 700°C. The ASR value of the uncoated sample increased significantly from 22 mΩ cm^2 to 310 mΩ cm^2 after the 100-h oxidation at 700°C. In contrast, the value of the coated sample was very stable. The ASR for the coated sample decreased slightly from 24 mΩ cm^2 to 21 mΩ cm^2 over the first 40 h. This may be due to better sintering of the silver paste and silver wire. This effect is also visible for the uncoated sample, when the increase in the ASR seems slower than after this time period. For the coated sample, the ASR increased from 20 mΩ cm^2 to 22 mΩ cm^2 from 50 h to 100 h. Clearly, the EPD-coated sample exhibited significantly superior ASR performance compared with the uncoated sample. This highlights the ability of the AC EPD process to deposit coatings on all surfaces of the porous substrate and significantly reduce the rate of further oxidation of the sample.

Figure 8a and b shows the microstructure of uncoated and coated samples after oxidation testing. The Cr concentration was measured quantitatively by EDS line scanning. Figure 8c and d shows the Cr concentration profiles for uncoated and coated samples after the 100-h oxidation test. The thickness of Cr_2O_3 for the uncoated sample after oxidation is around 1.8 μm. The thickness of Cr_2O_3 for the coated sample after oxidation at the surface is around 1 μm. There is a preformed Cr_2O_3 layer in the coated sample before the oxidation test, during the densification anneal at 950°C, before the coating has fully densified. Therefore, the growth rate of the TGO for the coated sample is much slower than for the uncoated sample. The TGA results show that the EPD coating layer on porous SUS430 substrate effectively limited Cr_2O_3 layer growth.

CONCLUSIONS

Deposition of protective $CuNi_{0.2}Mn_{1.8}O_4$ spinel coatings on porous metallic substrates was studied. $CuNi_{0.2}Mn_{1.8}O_4$ spinel powder was made by the glycine-nitrate process and deposited on porous SUS430 substrates using AC EPD. As-deposited samples were densified by a two-step densification anneal consisting of reduction in H_2 at 950°C for 2 h then reoxidation at 750°C for 24 h in air. Oxidation tests at 700°C in air were carried out for 100 h. TGA measurements showed that the oxidation rate constant k_g was 2.25×10^{-6} mg^2 cm^{-4} s^{-1} for uncoated sample and 9.0×10^{-8} mg^2 cm^{-4} s^{-1} for the coated sample, indicating that the coating reduced the k_g value by a factor of 25. ASR measurements revealed an increase from 22 mΩ cm^2 to 310 mΩ cm^2 for the uncoated sample. In contrast, the ASR of the coated sample remained very stable and increased to only 25 mΩ cm^2. EDS line scans showed that the thickness of Cr_2O_3 for the uncoated sample after oxidation was around 1.8 μm, in contrast to 1.0 μm for the coated sample, most of which formed during the two-step densification anneal. The TGA, ASR, and EDS line scan results are consistent. The results confirm the significant positive effect of the EPD coating layer on protecting the porous SUS430 substrate from oxidation and keeping the ASR value low.

ACKNOWLEDGEMENTS

This work was supported, in part, by a grant from Nissan Technical Center North America (NTCNA). The authors acknowledge Prof. Mark Horenstein and Neeraj Basu for help with circuit design and fabrication of the AC deposition apparatus, and Dr. Zhihao Sun, Michelle Sugimoto, Jillian Rix, and Ben Levitas for experimental assistance.

CONFLICT OF INTEREST

On behalf of all authors, the corresponding author states that there are no conflicts of interest.

REFERENCES

1. T. Brylewski, M. Nanko, T. Maruyama, and K. Przybylski, *Solid State Ionics* 143, 131. (2001).
2. J. Wu, and X. Liu, *J. Mater. Sci. Technol.* 26, 293. (2010).
3. I. Antepara, I. Villarreal, L. Rodríguez-Martínez, N. Lecanda, U. Castro, and A. Laresgoiti, *J. Power Sources* 151, 103. (2005).
4. S. Molin, B. Kusz, M. Gazda, and P. Jasinski, *J. Power Sources* 181, 31. (2008).
5. M. Haydn, K. Ortner, T. Franco, N. Menzler, A. Venskutonis, and L. Sigl, *Powder Metall.* 56, 382. (2013).
6. N. Sakai, T. Horita, Y.P. Xiong, K. Yamaji, H. Kishimoto, M.E. Brito, H. Yokokawa, and T. Maruyama, *Solid State Ionics* 176, 681. (2005).
7. H. Kurokawa, K. Kawamura, and T. Maruyama, *Solid State Ionics* 168, 13. (2004).
8. S. Badwal, R. Deller, K. Foger, Y. Ramprakash, and J. Zhang, *Solid State Ionics* 99, 297. (1997).
9. L. Blum, W.A. Meulenberg, H. Nabielek, and R. Steinberger-Wilckens, *Int. J. Appl. Ceram. Technol.* 2, 482. (2005).
10. H. Yokokawa, H. Tu, B. Iwanschitz, and A. Mai, *J. Power Sources* 182, 400. (2008).
11. X. Chen, *Int J. Hydrogen Energy* 39, 505. (2014).
12. R. Wang, M. Würth, U.B. Pal, S. Gopalan, and S.N. Basu, *J. Power Sources* 360, 87. (2017).
13. R. Wang, U.B. Pal, S. Gopalan, and S.N. Basu, *J. Electrochem. Soc.* 164, F740. (2017).
14. M.A. Uddin, A. Aphale, B. Hu, S.J. Heo, U. Pasaogullari, and P. Singh, *J. Electrochem. Soc.* 164, F1342. (2017).
15. S.J. Heo, J. Hong, A. Aphale, B. Hu, and P. Singh, *J. Electrochem. Soc.* 166, F990. (2019).
16. Z. Zhu, M. Sugimoto, U. Pal, S. Gopalan, and S. Basu, *J. Power Sources,* 471, 228474, (2020).
17. Z. Zhu, M. Sugimoto, U. Pal, S. Gopalan, and S. Basu, *J. Power Sources Adv.,* 6, 100037, (2020).
18. L. Besra, and M. Liu, *Prog. Mater. Sci.* 52, 1. (2007).
19. M. Galbo, K.J. Yoon, U.B. Pal, S. Gopalan, and S.N. Basu, *Energy Technol.* 2015, 337. (2015).
20. T. Uehara, N. Yasuda, M. Okamoto, and Y. Baba, *J. Power Sources* 196, 7251. (2011).
21. H. Zhang, Z. Zhan, and X. Liu, *J. Power Sources* 196, 8041. (2011).
22. H. Abdoli, and P. Alizadeh, *Mater. Lett.* 80, 53. (2012).
23. A. Petric, and H. Ling, *J. Am. Ceram. Soc.* 90, 1515. (2007).
24. S. Joshi, and A. Petric, *Int. J. Hydrogen Energy* 42, 5584. (2017).
25. Z. Sun, S. Gopalan, U.B. Pal, and S.N. Basu, *Energy Technol.* 2019, 265. (2019).
26. A. Chávez-Valdez, and A.R. Boccaccini, *Electrochim. Acta* 65, 70. (2012).
27. M. Ammam, *RSC Adv.* 2, 7633. (2012).
28. L.A. Chick, L. Pederson, G. Maupin, J. Bates, L. Thomas, and G. Exarhos, *Mater. Lett.* 10, 6. (1990).
29. Z. Sun, S. Gopalan, U.B. Pal, and S.N. Basu, *Surf. Coat. Technol.* 323, 49. (2017).
30. Z. Sun, R. Wang, A.Y. Nikiforov, S. Gopalan, U.B. Pal, and S.N. Basu, *J. Power Sources* 378, 125. (2018).
31. N. Hosseini, M. Abbasi, F. Karimzadeh, and G. Choi, *J. Power Sources* 273, 1073. (2015).
32. L. Chen, E.Y. Sun, J. Yamanis, and N. Magdefrau, *J. Electrochem. Soc.* 157, B931. (2010).